Research Article

Nano Research
2022, 15(10): 8908–8913

ISSN 1998-0124 CN 11-5974/O4
https://doi.org/10.1007/s12274-022-4812-6

Homoleptic alkynyl-protected Ag_{32} nanocluster with atomic precision: Probing the ligand effect toward CO_2 electroreduction and 4-nitrophenol reduction

Leyi Chen[1,§], Fang Sun[2,§], Quanli Shen[1], Lubing Qin[1], Yonggang Liu[1], Liang Qiao[3], Qing Tang[2] (✉), Likai Wang[4] (✉), and Zhenghua Tang[1,5] (✉)

[1] *New Energy Research Institute, School of Environment and Energy, South China University of Technology, Guangzhou Higher Education Mega Centre, Guangzhou 510006, China*
[2] *School of Chemistry and Chemical Engineering, Chongqing Key Laboratory of Theoretical and Computational Chemistry, Chongqing University, Chongqing 401331, China*
[3] *China Petrochemical Research Institute, PetroChina Company Limited, Beijing 102206, China*
[4] *School of Chemistry and Chemical Engineering, Shandong University of Technology, Zibo 255049, China*
[5] *Guangdong Provincial Key Laboratory of Functional Supramolecular Coordination Materials and Applications, Jinan University, Guangzhou 510632, China*
[§] *Leyi Chen and Fang Sun contributed equally to this work.*

Received: 12 June 2022 / **Revised:** 24 July 2022 / **Accepted:** 25 July 2022

ABSTRACT

We report a superatomic homoleptic alkynyl-protected $Ag_{32}L_{24}$ (L = 3,5-bis(trifluoromethylbenzene) acetylide, Ag_{32} for short) nanocluster with atomic precision, which possesses eight free electrons. Ag_{32} is formed by an Ag_{17} core with C_3 symmetry and the remaining 15 Ag atoms bond to each other and coordinate with the 24 surface ligands. When applied as electrocatalyst for CO_2 reduction reaction (CO_2RR), Ag_{32} exhibited the highest Faradaic efficiency (FE) of CO up to 96.44% at −0.8 V with hydrogen evolution being significantly suppressed in a wide potential range, meanwhile it has a reaction rate constant of 0.242 min^{-1} at room temperature and an activation energy of 45.21 $kJ·mol^{-1}$ in catalyzing the reduction of 4-nitrophenol, both markedly superior than the thiolate and phosphine ligand co-protected Ag_{32} nanocluster. Such strong ligand effect was further understood by density functional theory (DFT) calculations, as it revealed that, one single ligand stripping off from the intact cluster can create the undercoordinated Ag atom as the catalytically active site for both clusters, but alkynyl-protected Ag_{32} nanocluster possesses a smaller energy barrier for forming the key *COOH intermediate in CO_2RR, and favors the adsorption of 4-nitrophenol. This study not only discovers a new member of homoleptic alkynyl-protected Ag nanocluster, but also highlights the great potentials of employing alkynyl-protected Ag nanoclusters as bifunctional catalysts toward various reactions.

KEYWORDS

Ag_{32} nanocluster, alkynyl ligand, ligand effect, CO_2 electroreduction, 4-nitrophenol reduction

1 Introduction

As a novel type of nanomaterial, coinage metal nanoclusters possess ultrasmall size of 1–3 nm and can be chemically synthesized with atomic precision. The ultrasmall size endows metal nanoclusters with strong quantum confinement effect [1]. Thanks to the size-dependent optical property, unique electronic structure, and readily modifiable surface ligand, atomically precise metal nanoclusters have found versatile applications in catalysis, electronic, biosensing, biomedical treatment, and so on [2–4]. Currently, the most widely employed ligand is thiolate molecules, and until so far, more than 200 thiolate protected coinage metal (alloy) nanoclusters have been structurally resolved by single crystal X-ray diffraction (SC-XRD) [5–13]. Recently, great research attentions have been devoted to preparing alkynyl-protected metal nanoclusters, as alkynyl molecules can bind to the metal surface with σ and/or π bonding, leading to more diverse interfacial bonding moieties hence drastically different physicochemical properties and functionalities can be realized for alkynyl-protected metal nanoclusters [14–16]. More importantly, once the triple bond of the alkynyl ligand is connected with the cluster kernel, the highly conjugated structure is favorable for electron shuttling, which is beneficial for promoting the catalytic performance in a variety of reactions. For instance, Wan et al. reported the strong ligand effect of the semi-hydrogenation of alkynes catalyzed by $[Au_{38}(L)_{20}(Ph_3P)_4]^{2+}$ (L = alkynyl or thiolate) cluster, in which alkynyl-protected Au_{38} has overwhelmingly higher conversion of the reaction substrate than the thiolate stabilized Au_{38} (> 97% vs. < 2%) [17]. Such ligand effect was also observed in hydrogen evolution reaction (HER) catalyzed by Au_{25} nanoclusters reported by Tsukuda group, in which the onset potential of $Au_{25}(C{\equiv}CAr^F)_{18}$ is about 70 mV positive than that of $Au_{25}(SC_2H_4Ph)_{18}$ [18]. Recently, our group successfully prepared

Address correspondence to Zhenghua Tang, zhht@scut.edu.cn; Qing Tang, qingtang@cqu.edu.cn; Likai Wang, lkwangchem@sdut.edu.cn

the all-alkynyl-protected $Ag_{15}(C{\equiv}C^tBu)_{12}$ cluster, and in the electrochemical CO_2 reduction reaction (CO_2RR), it can convert CO_2 into CO exclusively with the highest Faradaic efficiency (FE) of CO reaching ~ 95%, superior to other ligands stabilized Ag nanomaterials [19]. This study also demonstrates that, alkynyl-protected Ag nanoclusters might have some unexpected exceptional catalytic activity.

It is worth noting that, in the past a few years, significant progress toward controllable synthesis and structure analysis has been achieved on homoleptic alkynyl-protected Au nanoclusters. Until so far, the crystal structure and optical property of Au_{22} [20], Au_{23} [21], Au_{25} [22], Au_{36} [23], Au_{44} [24], Au_{50} [25], Au_{99} [26], Au_{110} [27], and Au_{144} [28] nanoclusters have been documented. Compared with the great breakthroughs in Au nanoclusters, the study of homoleptic alkynyl-protected Ag nanoclusters lags behind. In 2017, Li and Zhang groups reported the first all-alkynyl-protected Ag cluster of $Ag_{74}(C{\equiv}CPh)_{44}$, which possesses a $Ag_4@Ag_{22}@Ag_{48}$ three shell metal-core structure [29]. In 2018, Xie and Lu groups documented the all-alkynyl-protected $Ag_{51}(C{\equiv}C^tBu)_{32}$ molecule, and its fluorescence exhibits a strong solvatochromic effect [30]. Plus the above mentioned $Ag_{15}(C{\equiv}C^tBu)_{12}$ cluster reported by our group, it can be seen that, the cases of homoleptic alkynyl-protected Ag nanoclusters are quite limited. This is probably due to that, compared to Au, Ag is more susceptible to oxidation in the presence of oxygen, leading to the preparation of stable Ag nanoclusters with full alkynyl protection is much more challenging. Nevertheless, considering Ag is much cheaper than Au, and Ag nanoclusters hold great potentials in various fields especially in the catalytic regime, hence enriching the members of homoleptic alkynyl-protected Ag nanoclusters and exploring their catalytic performance is of fundamental interests and practical value. Actually, this is the primary goal and aim of our current investigation.

Herein, we report a new homoleptic alkynyl-protected Ag nanocluster superatom of $Ag_{32}(C{\equiv}CAr)_{24}$ with eight free electrons. It is a racemate with a C_3 symmetric Ag_{17} nucleus in the Ag_{32} kernel, and it possesses four types of ligand-metal bonding motifs. Remarkably, it demonstrates superior catalytic performance in both CO_2RR and 4-nitrophenol reduction than the $[Ag_{32}(DPPE)_5(SC_6H_4CF_3)_{24}]^{2-}$ molecule co-protected by thiolate and phosphine ligands, evidenced by the markedly higher CO Faradaic efficiency and partial current density as well as stronger capability to inhibit H_2 generation in CO_2RR, and much higher reaction rate in 4-nitrophenol reduction. Density functional theory (DFT) calculations disclosed that releasing one complete ligand from the cluster to expose undercoordinated Ag atom is the catalytically active center for both clusters, but alkynyl-protected Ag_{32} nanocluster possesses lower thermodynamic barrier to form the key COOH* intermediate during CO_2RR compared with H_2 formation toward HER and also favors the adsorption of 4-nitrophenol.

2 Results and discussion

Slightly different from the conventional co-reduction method, Ag_{32} nanocluster was synthesized by adding both CF_3CO_2Ag and $NaBH_3CN$ into a methanol solution with CH_3ONa and alkynyl ligand (the synthetic details can be found in the Electronic Supplementary Material (ESM)). About a week later, purplish black block crystals were obtained, and the image of crystals under an optical microscope is shown in Fig. S1 in the ESM.

The total structure of the Ag_{32} nanocluster was then analyzed by SC-XRD. It reveals that, Ag_{32} nanocluster as a racemate crystallizes in a triclinic unit cell in the *P*1 space group (Fig. S2 and Table S1 in the ESM), with a monolayer composed of 24 alkynyl ligands protecting the metal core. The diagram of Ag_{32} enantiomers with mirror symmetry can be found in Fig. S3 in the ESM. Figure 1 shows the overall structure of Ag_{32} nanocluster, and it behaves electrically neutral. The 32 Ag atoms in the metal core can be divided into a $Ag_5@Ag_{12}$ kernel structure connected with the remaining 15 Ag atoms, and its anatomy is illustrated in Fig. 2. An Ag_5 is formed by two Ag_4 tetrahedra sharing the Ag_3 plane (Fig. 2(a), indicated in green), and the average Ag–Ag bond length is 2.894 Å, similar to the conventional Ag–Ag bond length (2.88 Å). Note that, the three Ag atoms in the Ag_3 shared plane are not connected with any alkynyl ligands. On the top and bottom vertices of Ag_5, there are two hexagons A and B each containing six Ag atoms (Fig. 2(b), indicated in yellow), that is, 12 Ag atoms are capped onto Ag_5. Meanwhile, two Ag_6 hexagons interact with each other through two Ag–Ag bonds with bond lengths of 2.960 and 2.984 Å, respectively, constituting a hexagon with a concave center (Fig. 2(c), indicated in purple). The Ag–Ag bond lengths in Ag_{17} kernel range from 2.687–3.562 Å, with an average value of 2.988 Å. There are two Ag atoms on the top-side and bottom-side of the two Ag_6 hexagons, respectively (Fig. 2(d), indicated in pink), each of which is connected to A/B through four Ag–Ag bonds with the average Ag–Ag distance of 3.049 Å. Meanwhile, there are four Ag atoms along the waist of the Ag_{17} kernel (Fig. 2(d), indicated in purple), and each Ag atom is connected with Ag_{17} by five Ag–Ag bonds with an average distance of 3.074 Å. Two Ag_3 sharing one edge form a Ag_4, while two Ag_4 share a vertex Ag atom, and these 7 Ag atoms are also located at the waist (Figs. 2(e) and 2(f), indicated in yellow). Influenced by the interaction with ligands, the average value of Ag–Ag distance between the 7 Ag atoms and Ag_{17} becomes slightly elongated (3.162 Å).

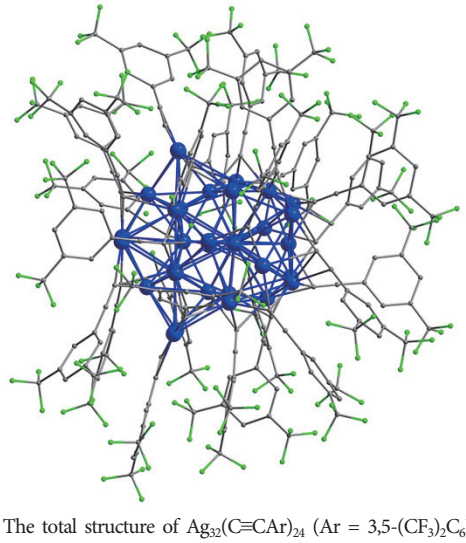

Figure 1 The total structure of $Ag_{32}(C{\equiv}CAr)_{24}$ (Ar = 3,5-$(CF_3)_2C_6H_3$). Color code: Ag, blue; C, gray; and F, green. All hydrogen atoms are omitted for clarity.

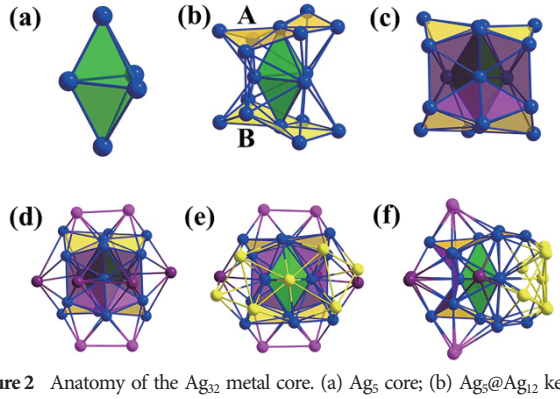

Figure 2 Anatomy of the Ag_{32} metal core. (a) Ag_5 core; (b) $Ag_5@Ag_{12}$ kernel; (c) left view of Ag_{17} kernel; (d) Ag_{17} + Ag_4 + Ag_4; (e) left view of Ag_{32}; and (f) front view of Ag_{32}. Color code: Ag, blue/pink/purple/yellow.

Interestingly, as demonstrated in Fig. S4 in the ESM, the Ag_{17} kernel shows C_3 symmetry in whole, reminiscent of the R/S-Ag_{17} nuclear structure reported by Zang group [31]. It is well known that, chirality arising in an achiral environment originates from three sources, in which the chirality of most nanoclusters are induced by chiral ligands [32, 33], while some nanoclusters' chirality are generated by chiral arrangement of internal metal atoms [34]. In addition, chirality can also result from rotation or twisting of the metal core [35]. On the premise of the above-mentioned metal core structure analysis and the non-chiral ligands, it can be concluded that, the chirality of Ag_{32} nanocluster is probably from the chiral arrangement of internal Ag atoms.

Furthermore, the 24 alkynyl ligands are connected to the metal core with four bonding motifs (Fig. 3(a)). As demonstrated in Fig. 3(b), Motif A adopts μ_2–η^1, η^1 connection mode, and all the purple Ag atoms coordinate with the ligand in this mode, with four A motifs in total. Motif B belongs to the μ_2–η^1, η^2 linkage mode, that is, one of the Ag atoms interacts with the ligand by π bond and σ bond, in which the four pink Ag atoms are paired with ligands in this way. Motif C has one more key Ag atoms than Motif A with μ_3–η^1, η^1, and η^1 bonding modes, and two-thirds of the 24 ligands bond to Ag atoms by this motif (16 Motif C). Further, μ_3–η^1, η^2, η^2 bonding mode was adopted on Motif D, in which the ligands are connected with the yellow Ag atoms. Same with Motif B, there are two D motifs in total in the nanocluster. The detailed distribution arrangement of the 24 alkynyl ligands can be found in Fig. S5 in the ESM.

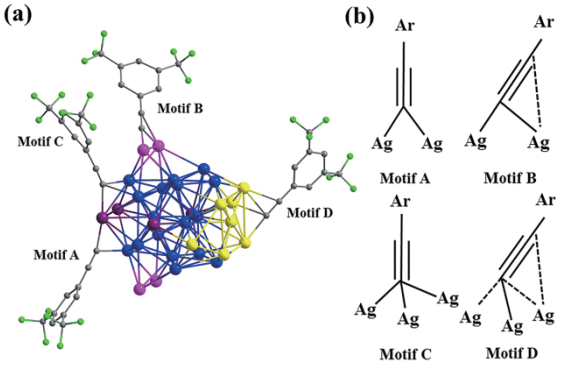

Figure 3 (a) Four types of ligand-metal bonding motifs in Ag_{32}. Color code: Ag, blue/pink/purple/yellow; C, gray; and F, green; (b) four motifs in Ag_{32} coordination modes for alkynyl ligands.

The molecular composition of Ag_{32} nanocluster was further verified by electrospray ionization mass spectrometry (ESI-MS). The ESI-MS spectra (Fig. S6 in the ESM) show that, the main peak located at m/z = 4,539.53 Da can be assigned to $[Ag_{33}(C{\equiv}CAr)_{23}(CH_3O)Cl]^{2-}$ (Cal. M_W: 4,539.59 Da). The presence of CH_3O^- is probably due to the using of methanol as solvent in the MS measurement, and dichloromethane may be the source of Cl^- during single crystal growth [36]. In addition, the isotopic distribution of Ag_{32} nanocluster is in good agreement with the fitting results (inset in Fig. S6 in the ESM). X-ray photoelectron spectroscopy (XPS) was next employed to further probe the electronic structure of the nanocluster. The survey-scan spectrum in Fig. S7(a) in the ESM validated the presence of the essential elements. The high resolution Ag 3d XPS spectrum in Fig. S7(b) in the ESM shows that, the binding energy of Ag $3d_{5/2}$ is 368.7 eV, indicating the valence state of Ag in Ag_{32} nanocluster is closer to Ag(0) (368.6 eV) [37].

Next, the optical absorbance of Ag_{32} nanocluster was examined. Ag_{32} can be easily dissolved in CH_2Cl_2, and presents as a purple solution (inset in Fig. 4). As demonstrated in Fig. 4, Ag_{32} exhibits characteristic absorption feature. There is a strong absorption peak

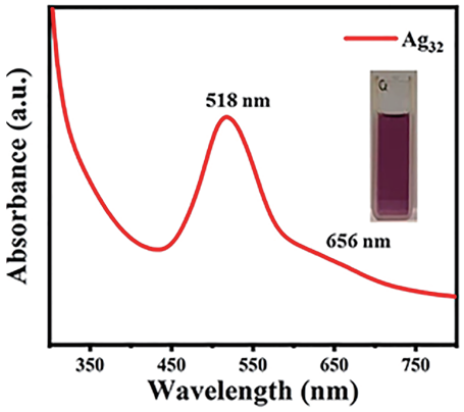

Figure 4 Ultraviolet–visible (UV–vis) absorbance spectrum of Ag_{32}. Inset: photograph of the cluster in CH_2Cl_2.

at 518 nm along with a relatively weak shoulder appearing at 656 nm.

The catalytic performance toward electrochemical CO_2 reduction (CO_2RR) of the Ag_{32} nanocluster was then studied and compared with that of $[Ag_{32}(DPPE)_5(SR)_{24}]^{2-}$ nanocluster under the same conditions to probe the ligand effect. $[Ag_{32}(DPPE)_5(SR)_{24}]^{2-}$ nanocluster was synthesized by following the previously reported method [38], and its total structure is shown in Fig. S8(a) in the ESM. It also adopts a Ag_{17} kernel with a Ag_5 unit capping on it (Fig. S8(b) in the ESM), forming a Ag_{22} kernel. In addition, there are four Ag atoms at the waist of Ag_{22} (green polyhedra) and two Ag atoms at the bottom (green polyhedra) together forming the $Ag_6(DPPE)_3(SR)_{12}$ unit, and four Ag atoms (blue polyhedra) forming two $Ag_2(DPPE)(SR)_4$ motifs at the top (Figs. S8(c) and S8(d) in the ESM). $[Ag_{32}(DPPE)_5(SR)_{24}]^{2-}$ shows a characteristic absorbance feature with an apparent peak at ~ 477 nm, and three shoulders above 500 nm (Fig. S9 in the ESM). Its composition was further verified by ESI-MS measurement. As illustrated in Fig. S10 in the ESM, the most intense peak with m/z at 5,204.18 Da is assigned to $[M+Ag(DPPE)(SR)+CH_3OH]^{2-}$ (Cal. 5,204.34 Da), while the neighboring peak located at m/z = 5,061.23 Da is attributed to $[M+DPPE+CH_3OH]^{2-}$ (Cal. 5,061.38 Da). The presence of CH_3OH is probably due to that it is the solvent in MS measurement.

The CO_2RR performance comparison of Ag_{32} and $[Ag_{32}(DPPE)_5(SR)_{24}]^{2-}$ clusters is shown in Fig. 5. CO and H_2 are the main products for both clusters. As illustrated in Figs. 5(a) and 5(b), the total Faradaic efficiency of CO + H_2 can reach 100% in the potential range of (−0.7, −1.1) and (−0.8, −1.1) V for Ag_{32} and $[Ag_{32}(DPPE)_5(SR)_{24}]^{2-}$, respectively. However, in all the tested potentials, the FE_{CO} value of Ag_{32} is higher than that of $[Ag_{32}(DPPE)_5(SR)_{24}]^{2-}$. The highest FE_{CO} is 96.44% at −0.8 V for Ag_{32}, while in sharp contrast, only a maximum of 56.67% can be achieved at −1.0 V for $[Ag_{32}(DPPE)_5(SR)_{24}]^{2-}$. Correspondingly, the FE_{H_2} is less than 10% in the potential range of (−0.7, −0.9) V for Ag_{32}, indicating HER is significantly suppressed by Ag_{32}, while for $[Ag_{32}(DPPE)_5(SR)_{24}]^{2-}$, the FE_{H_2} value is above 50% in the potential range of (−0.7, −1.1) V with a maximal value of 68.91% at −0.8 V. Figure 5(c) shows that, the partial current density of CO keeps increasing as the potential goes more negatively, and the highest current density can reach 9.05 mA·cm^{-2} for Ag_{32}, while the partial current density of H_2 increases continuously but cannot exceed that of CO. Such change trend was also observed in both CO and H_2 for $[Ag_{32}(DPPE)_5(SR)_{24}]^{2-}$, and the current densities of CO and H_2 are comparable in all tested potentials (Fig. 5(d)). Interestingly, despite the homoleptic alkynyl-protected Ag_{32} cluster exhibited remakably superior CO_2RR activity to the

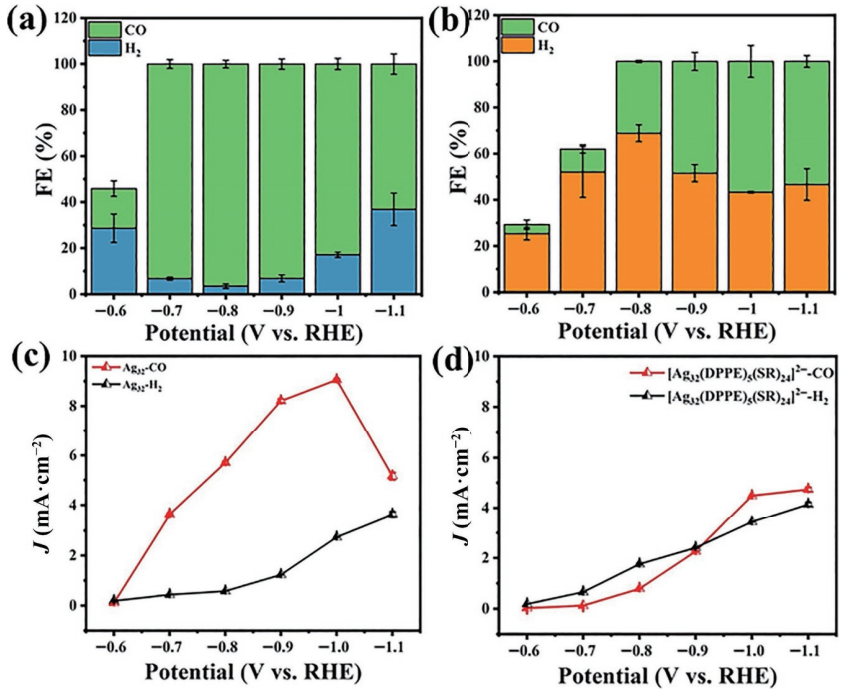

Figure 5 Faradaic efficiency of CO and H_2 for (a) Ag_{32} and (b) $[Ag_{32}(DPPE)_5(SR)_{24}]^{2-}$ at different voltages. Partial current densities of CO and H_2 for (c) Ag_{32} and (d) $[Ag_{32}(DPPE)_5(SR)_{24}]^{2-}$ at different voltages (electrolyte: 0.5 M $NaHCO_3$).

$[Ag_{32}(DPPE)_5(SR)_{24}]^{2-}$ molecule, both clusters demonstrated rather similar but robust long-term stability, manifested by the slight current density decay in 15 h's continuous operation (Fig. S11 in the ESM).

Subsequently, we conducted DFT calculations to unravel the reaction mechanism of CO_2RR to CO vs. HER (see the ESM for computational details). To simplify the calculation, all –C≡C–Ar, DPPE, and $-SC_6H_4CF_3$ ligands were replaced with more computationally tractable $-C{\equiv}C-CH_3$, $P_2C_2H_6$, and $-SCH_3$, respectively. The free energy profile predicts that, both the intact $Ag_{32}(C{\equiv}C-CH_3)_{24}$ and $[Ag_{32}(P_2C_2H_6)_5(SCH_3)_{24}]^{2-}$ are electrochemically inactive with extremely large free energy barrier of 1.28 and 1.23 eV (Fig. 6(a) and Table S2 in the ESM), which are inconsistent with the experimental results. In contrast, when a single alkynyl ligand or thiolate is removed from the NC, it decreases the thermodynamic barrier for COOH* formation (0.40 and 0.50 eV), and thus significantly accelerates the CO_2RR (red and green paths in the green region, Fig. 6(a)). The optimized adsorption geometries of reaction species are depicted in Figs. 6(b)–6(g). Either removing –C≡CR or –SR creates the Ag atom as the active site for both nanocluster models. Although they were revealed to hold comparable endothermic (up-hill) COOH* formation, the alkynyl ligand removed $[Ag_{32}(C{\equiv}C-CH_3)_{23}]^+$ has a larger thermodynamic barrier for H_2 formation from adsorbed H* (0.51 eV) compared with the –SR removed $[Ag_{32}(P_2C_2H_6)_5(SCH_3)_{23}]^-$ (0.05 eV), indicating a higher CO_2RR to CO selectivity for exposed Ag atom site by removing the $-C{\equiv}C-CH_3$ ligand.

The catalytic properties of the two clusters were further compared by catalyzing the reduction of 4-nitrophenol into 4-aminophenol at the same conditions [39]. Both catalysts were loaded with TiO_2, and the absorbance change was *in-situ* monitored [40]. As shown in Fig. S12(a) in the ESM, in the presence of Ag_{32}/TiO_2 catalyst, $NaBH_4$ can completely reduce 4-nitrophenol in only 10 min. In stark contrast, when $[Ag_{32}(DPPE)_5(SR)_{24}]^{2-}/TiO_2$ or TiO_2 was used as catalyst, the concentration of the reactants exhibited negligible change after 4 h (Figs. S12(b) and S12(c) in the ESM), indicating extremely weak catalytic activity for both. Alkynyl-protected Ag_{32} nanocluster

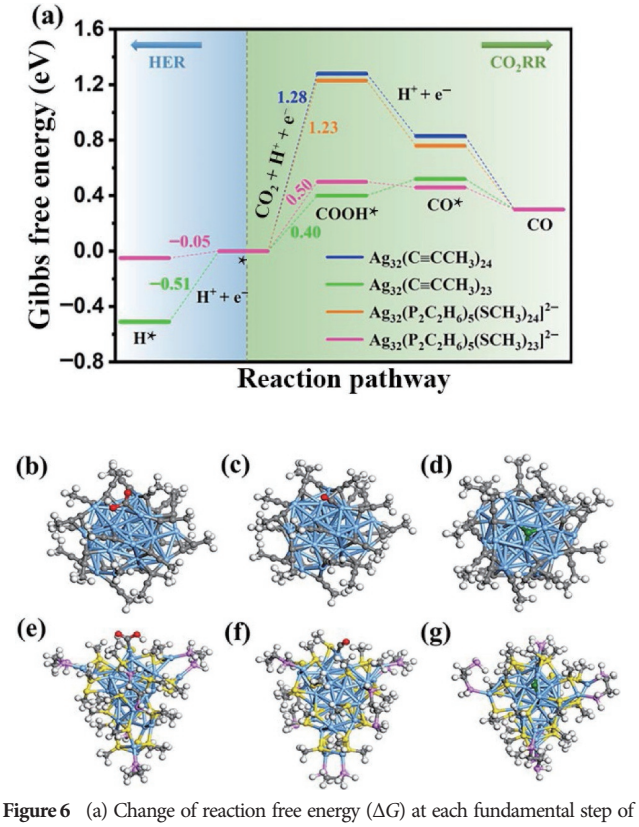

Figure 6 (a) Change of reaction free energy (ΔG) at each fundamental step of CO_2RR and HER for two nanoclusters and the stripping of one intact ligand each. Adsorption structure of COOH*, CO*, and H* intermediates on ((b)–(d)) $[Ag_{32}(C{\equiv}C-CH_3)_{23}]^+$ and ((e)–(g)) $[Ag_{32}(P_2C_2H_6)_5(SCH_3)_{23}]^-$. Color code: Ag, blue; C, gray; O, red; S, yellow; P, pink; H*, green; and other H, white.

possessed markedly superior catalytic activity, in good echo with the strong ligand effect observed in CO_2RR. Furthermore, $\ln(C_t/C_0)$ versus time exhibits an excellent linear relationship (Fig. 7(a)), suggesting a first-order reaction kinetics was adopted. The reaction rate constant of the Ag_{32}/TiO_2 catalyst was also calculated as 0.242 min^{-1} (room temperature). To further examine the intrinsic catalytic property of the Ag_{32}/TiO_2 catalyst, the reaction

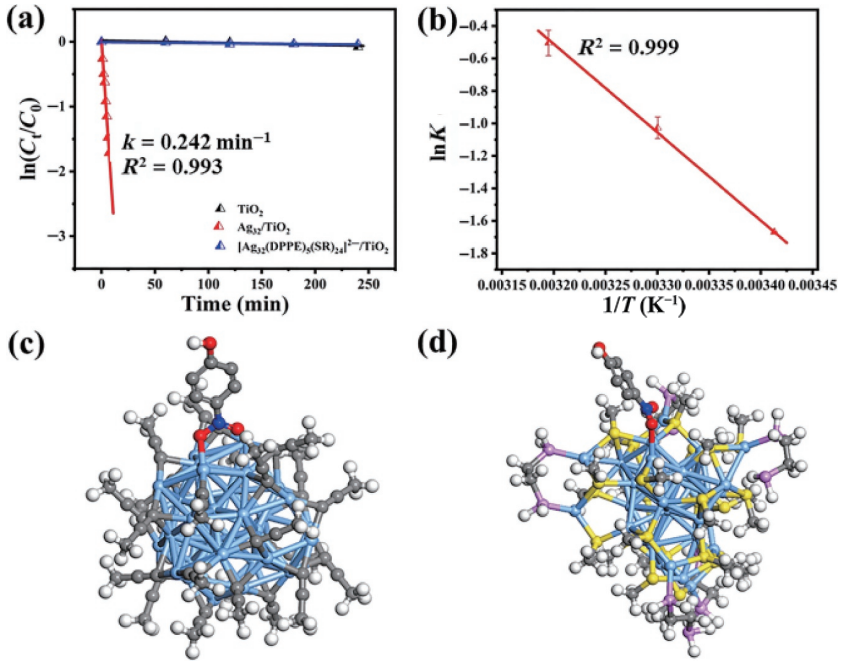

Figure 7 (a) $\ln(C_t/C_0)$ versus time chart of Ag_{32}/TiO_2 (red), $[Ag_{32}(DPPE)_5(SR)_{24}]^{2-}/TiO_2$ (blue), and TiO_2 (black) catalyst; (b) $\ln K$ versus $1/T$ diagram in the presence of Ag_{32}/TiO_2 catalyst. The adsorption structure of 4-nitrophenol on (c) $[Ag_{32}(C{\equiv}C{-}CH_3)_{23}]^+$ and (d) $[Ag_{32}(P_2C_2H_6)_5(SCH_3)_{23}]^-$.

was conducted at different temperatures (20, 30, and 40 °C). Figure S13 in the ESM shows that, it takes 13, 8, and 5 min to complete the reaction at the above temperature, respectively, and the k value is 0.189, 0.358, and 0.604 min^{-1} in sequence (Fig. S14 in the ESM). The natural log of the reaction rate constant was plotted as a function of reverse time, and an excellent linear regression was obtained (Arrhenius equation). The activation energy (E_a) of the Ag_{32}/TiO_2 catalyst was then calculated as 45.21 $kJ{\cdot}mol^{-1}$ (Fig. 7(b)), which is lower than that of CTAB-stabilized gold nanoparticles (48 ± 2 $kJ{\cdot}mol^{-1}$) [41] and silver nanoparticles synthesized on procyanidin-grafted eggshell membranes (66.8 $kJ{\cdot}mol^{-1}$) [42].

The ligand effect of alkynyl vs. thiolate on 4-nitrophenol reduction is further understood by DFT calculations. We found that both fully ligand-protected clusters could not capture 4-nitrophenol, however, the removal of one ligand showed favorable adsorption adhesion. As illustrated in Figs. 7(c) and 7(d), the calculated adsorption Gibbs free energy of 4-nitrophenol on the exposed Ag atom of $[Ag_{32}(C{\equiv}C{-}CH_3)_{23}]^+$ is −2.92 eV, which is significantly much lower than that of $[Ag_{32}(P_2C_2H_6)_5(SCH_3)_{23}]^-$ (−1.74 eV). This suggests that the reduction of 4-nitrophenol is mainly affected by the removal of ligand, and 4-nitrophenol is more easily adsorbed on Ag_{32}/TiO_2, thus accounts for the superior activity.

3 Conclusions

In conclusion, we have successfully synthesized a new atomically precise Ag nanocluster superatom of $Ag_{32}L_{24}$ with eight electron closed electronic structure. It has characteristic optical absorbance feature, and possesses a $Ag_5@Ag_{12}$ kernel with the remaining 15 Ag atoms connected with the 24 surface ligands. Intriguingly, it exhibits markedly superior catalytic performance in both CO_2 electroreduction and the reduction of 4-nitrophenol than the thiolate and phosphine ligands co-protected Ag_{32} counterpart. DFT calculations disclosed that, one ligand removal to expose the shell Ag atom acts as the active site for both clusters, but alkynyl-protected Ag_{32} nanocluster possesses a higher CO selectivity and stronger adsorption of 4-nitrophenol. This study not only enriches the family members of molecular homoleptic alkynyl-protected Ag nanoclusters, but also highlights the unique advantages of employing alkynyl ligand to prepare coinage metal nanoclusters with enhanced catalytic activity and improved stability for various reactions and beyond.

Acknowledgements

This study was supported by the Open Fund of Guangdong Provincial Key Laboratory of Functional Supramolecular Coordination Materials and Applications (No. 2021A07). Z. H. T. acknowledges the financial support from Guangdong Natural Science Funds (No. 2022A1515011840). L. K. W. acknowledges the funding from the National Natural Science Foundation of China (No. 21805170). Q. T. thanks the grants from the National Natural Science Foundation of China (No. 21903008) and the Chongqing Science and Technology Commission (No. cstc2020jcyj-msxmX0382).

Electronic Supplementary Material: Supplementary material (experimental details including the cluster synthesis, catalyst preparation, catalytic reaction measurements, computational details, and supporting figures) is available in the online version of this article at https://doi.org/10.1007/s12274-022-4812-6.

References

[1] Qian, H. F.; Zhu, M. Z.; Wu, Z. K.; Jin, R. C. Quantum sized gold nanoclusters with atomic precision. *Acc. Chem. Res.* **2012**, *45*, 1470–1479.

[2] Kawawaki, T.; Negishi, Y.; Kawasaki, H. Photo/electrocatalysis and photosensitization using metal nanoclusters for green energy and medical applications. *Nanoscale. Adv.* **2020**, *2*, 17–36.

[3] Kwak, K.; Lee, D. Electrochemistry of atomically precise metal nanoclusters. *Acc. Chem. Res.* **2019**, *52*, 12–22.

[4] Song, X. R.; Goswami, N.; Yang, H. H.; Xie, J. P. Functionalization of metal nanoclusters for biomedical applications. *Analyst* **2016**, *141*, 3126–3140.

[5] Jin, S.; Wang, S. X.; Song, Y. B.; Zhou, M.; Zhong, J.; Zhang, J.; Xia, A. D.; Pei, Y.; Chen, M.; Li, P. et al. Crystal structure and optical properties of the $[Ag_{62}S_{12}(SBu^t)_{32}]^{2+}$ nanocluster with a

complete face-centered cubic kernel. *J. Am. Chem. Soc.* **2014**, *136*, 15559–15565.

[6] Nan, Z. A.; Wang, Y.; Chen, Z. X.; Yuan, S. F.; Tian, Z. Q.; Wang, Q. M. Catalyzed assembly of hollow silver-sulfide cluster through self-releasable anion template. *Commun. Chem.* **2018**, *1*, 99.

[7] Chen, S.; Xiong, L.; Wang, S. X.; Ma, Z. Y.; Jin, S.; Sheng, H. T.; Pei, Y.; Zhu, M. Z. Total structure determination of $Au_{21}(S\text{-}Adm)_{15}$ and geometrical/electronic structure evolution of thiolated gold nanoclusters. *J. Am. Chem. Soc.* **2016**, *138*, 10754–10757.

[8] Das, A.; Li, T.; Nobusada, K.; Zeng, C. J.; Rosi, N. L.; Jin, R. C. Nonsuperatomic $[Au_{23}(SC_6H_{11})_{16}]^-$ nanocluster featuring bipyramidal Au_{15} kernel and trimeric $Au_3(SR)_4$ motif. *J. Am. Chem. Soc.* **2013**, *135*, 18264–18267.

[9] Crasto, D.; Malola, S.; Brosofsky, G.; Dass, A.; Häkkinen, H. Single crystal XRD structure and theoretical analysis of the chiral $Au_{30}S(S\text{-}t\text{-}Bu)_{18}$ cluster. *J. Am. Chem. Soc.* **2014**, *136*, 5000–5005.

[10] Bootharaju, M. S.; Joshi, C. P.; Parida, M. R.; Mohammed, O. F.; Bakr, O. M. Templated atom-precise galvanic synthesis and structure elucidation of a $[Ag_{24}Au(SR)_{18}]^-$ nanocluster. *Angew. Chem., Int. Ed.* **2016**, *55*, 922–926.

[11] Lin, X. Z.; Ma, W. G.; Sun, K. J.; Sun, B.; Fu, X. M.; Ren, X. Q.; Liu, C.; Huang, J. H. $[AuAg_{26}(SR)_{18}S]^-$ nanocluster:Open shell structure and high Faradaic efficiency in electrochemical reduction of CO_2 to CO. *J. Phys. Chem. Lett.* **2021**, *12*, 552–557.

[12] Yan, J. Z.; Su, H. F.; Yang, H. Y.; Malola, S.; Lin, S. C.; Häkkinen, H.; Zheng, N. F. Total structure and electronic structure analysis of doped thiolated silver $[MAg_{24}(SR)_{18}]^{2-}$ (M = Pd, Pt) clusters. *J. Am. Chem. Soc.* **2015**, *137*, 11880–11883.

[13] Wang, S. X.; Song, Y. B.; Jin, S.; Liu, X.; Zhang, J.; Pei, Y.; Meng, X. M.; Chen, M.; Li, P.; Zhu, M. Z. Metal exchange method using Au_{25} nanoclusters as templates for alloy nanoclusters with atomic precision. *J. Am. Chem. Soc.* **2015**, *137*, 4018–4021.

[14] Lei, Z.; Wan, X. K.; Yuan, S. F.; Guan, Z. J.; Wang, Q. M. Alkynyl approach toward the protection of metal nanoclusters. *Acc. Chem. Res.* **2018**, *51*, 2465–2474.

[15] Lei, Z.; Wan, X. K.; Yuan, S. F.; Wang, J. Q.; Wang, Q. M. Alkynyl-protected gold and gold-silver nanoclusters. *Dalton. Trans.* **2017**, *46*, 3427–3434.

[16] Ma, X. S.; Tang, Y.; Ma, G. Y.; Qin, L. B.; Tang, Z. H. Controllable synthesis and formation mechanism study of homoleptic alkynyl-protected Au nanoclusters: Recent advances, grand challenges, and great opportunities. *Nanoscale* **2021**, *13*, 602–614.

[17] Wan, X. K.; Wang, J. Q.; Nan, Z. A.; Wang, Q. M. Ligand effects in catalysis by atomically precise gold nanoclusters. *Sci. Adv.* **2017**, *3*, e1701823.

[18] Li, X.; Takano, S.; Tsukuda, T. Ligand effects on the hydrogen evolution reaction catalyzed by Au_{13} and $Pt@Au_{12}$: Alkynyl vs. *thiolate. J. Phys. Chem. C.* **2021**, *125*, 23226–23230.

[19] Qin, L. B.; Sun, F.; Ma, X. S.; Ma, G. Y.; Tang, Y.; Wang, L. K.; Tang, Q.; Jin, R. C.; Tang, Z. H. Homoleptic alkynyl-protected Ag_{15} nanocluster with atomic precision: Structural analysis and electrocatalytic performance toward CO_2 reduction. *Angew. Chem., Int. Ed.* **2021**, *60*, 26136–26141.

[20] Ito, S.; Takano, S.; Tsukuda, T. Alkynyl-protected $Au_{22}(C{\equiv}CR)_{18}$ clusters featuring new interfacial motifs and R-dependent photoluminescence. *J. Phys. Chem. Lett.* **2019**, *10*, 6892–6896.

[21] Guan, Z. J.; Hu, F.; Li, J. J.; Wen, Z. R.; Lin, Y. M.; Wang, Q. M. Isomerization in alkynyl-protected gold nanoclusters. *J. Am. Chem. Soc.* **2020**, *142*, 2995–3001.

[22] Li, J. J.; Guan, Z. J.; Lei, Z.; Hu, F.; Wang, Q. M. Same magic number but different arrangement: Alkynyl-protected Au_{25} with D_3 symmetry. *Angew. Chem., Int. Ed.* **2019**, *58*, 1083–1087.

[23] Ma, X. S.; Ma, G. Y.; Qin, L. B.; Chen, G. X.; Chen, S. W.; Tang, Z. H. A synchronous nucleation and passivation strategy for controllable synthesis of $Au_{36}(PA)_{24}$: Unveiling the formation process and the role of $Au_{22}(PA)_{18}$ intermediate. *Sci. China Chem.* **2020**, *63*, 1777–1784.

[24] Wan, X. K.; Guan, Z. J.; Wang, Q. M. Homoleptic alkynyl-protected gold nanoclusters: $Au_{44}(PhC{\equiv}C)_{28}$ and $Au_{36}(PhC{\equiv}C)_{24}$. *Angew. Chem., Int. Ed.* **2017**, *56*, 11494–11497.

[25] Guan, Z. J.; Hu, F.; Li, J. J.; Liu, Z. R.; Wang, Q. M. Homoleptic alkynyl-protected gold nanoclusters with unusual compositions and structures. *Nanoscale* **2020**, *12*, 13346–13350.

[26] Li, J. J.; Liu, Z. K.; Guan, Z. J.; Han, X. S.; Shi, W. Q.; Wang, Q. M. A 59-electron non-magic-number gold nanocluster $Au_{99}(C{\equiv}CR)_{40}$ showing unexpectedly high stability. *J. Am. Chem. Soc.* **2022**, *144*, 690–694.

[27] Wang, J. Q.; Shi, S.; He, R. L.; Yuan, S. F.; Yang, G. Y.; Liang, G. J.; Wang, Q. M. Total structure determination of the largest alkynyl-protected fcc gold nanocluster Au_{110} and the study on its ultrafast excited-state dynamics. *J. Am. Chem. Soc.* **2020**, *142*, 18086–18092.

[28] Ma, X. S.; Tang, Z. H.; Qin, L. B.; Peng, J.; Li, L. G.; Chen, S. W. Unravelling the formation mechanism of alkynyl protected gold clusters: A case study of phenylacetylene stabilized Au_{144} molecules. *Nanoscale* **2020**, *12*, 2980–2986.

[29] Qu, M.; Li, H.; Xie, L. H.; Yan, S. T.; Li, J. R.; Wang, J. H.; Wei, C. Y.; Wu, Y. W.; Zhang, X. M. Bidentate phosphine-assisted synthesis of an all-alkynyl-protected Ag_{74} nanocluster. *J. Am. Chem. Soc.* **2017**, *139*, 12346–12349.

[30] Duan, G. X.; Tian, L.; Wen, J. B.; Li, L. Y.; Xie, Y. P.; Lu, X. An atomically precise all-tert-butylethynide-protected Ag_{51} superatom nanocluster with color tunability. *Nanoscale* **2018**, *10*, 18915–18919.

[31] Zhang, M. M.; Dong, X. Y.; Wang, Z. Y.; Luo, X. M.; Huang, J. H.; Zang, S. Q.; Mak, T. C. W. Alkynyl-stabilized superatomic silver clusters showing circularly polarized luminescence. *J. Am. Chem. Soc.* **2021**, *143*, 6048–6053.

[32] Liu, W. D.; Wang, J. Q.; Yuan, S. F.; Chen, X.; Wang, Q. M. Chiral superatomic nanoclusters Ag_{47} induced by the ligation of amino acids. *Angew. Chem., Int. Ed.* **2021**, *60*, 11430–11435.

[33] Yang, H. Y.; Yan, J. Z.; Wang, Y.; Deng, G. C.; Su, H. F.; Zhao, X. J.; Xu, C. F.; Teo, B. K.; Zheng, N. F. From racemic metal nanoparticles to optically pure enantiomers in one pot. *J. Am. Chem. Soc.* **2017**, *139*, 16113–16116.

[34] Huang, J. H.; Wang, Z. Y.; Zang, S. Q.; Mak, T. C. W. Spontaneous resolution of chiral multi-thiolate-protected Ag_{30} nanoclusters. *ACS Cent. Sci.* **2020**, *6*, 1971–1976.

[35] Liu, C.; Li, T.; Abroshan, H.; Li, Z. M.; Zhang, C.; Kim, H. J.; Li, G.; Jin, R. C. Chiral Ag_{23} nanocluster with open shell electronic structure and helical face-centered cubic framework. *Nat. Commun.* **2018**, *9*, 744.

[36] Hu, F.; Li, J. J.; Guan, Z. J.; Yuan, S. F.; Wang, Q. M. Formation of an alkynyl-protected Ag_{112} silver nanocluster as promoted by chloride released *in situ* from CH_2Cl_2. *Angew. Chem., Int. Ed.* **2020**, *59*, 5312–5315.

[37] Wu, X. H.; Guo, Y. N.; Sun, Z. S.; Xie, F. H.; Guan, D. Q.; Dai, J.; Yu, F. J.; Hu, Z. W.; Huang, Y. C.; Pao, C. W. et al. Fast *operando* spectroscopy tracking *in situ* generation of rich defects in silver nanocrystals for highly selective electrochemical CO_2 reduction. *Nat. Commun.* **2021**, *12*, 660.

[38] Yang, H. Y.; Wang, Y.; Zheng, N. F. Stabilizing subnanometer Ag(0) nanoclusters by thiolate and diphosphine ligands and their crystal structures. *Nanoscale* **2013**, *5*, 2674–2677.

[39] Li, Y.; Tang, Z. H.; Prasad, P. N.; Knecht, M. R.; Swihart, M. T. Peptide-mediated synthesis of gold nanoparticles: Effects of peptide sequence and nature of binding on physicochemical properties. *Nanoscale* **2014**, *6*, 3165–3172.

[40] Guan, Z. J.; He, R. L.; Yuan, S. F.; Li, J. J.; Hu, F.; Liu, C. Y.; Wang, Q. M. Ligand engineering toward the trade-off between stability and activity in cluster catalysis. *Angew. Chem., Int. Ed.* **2022**, *61*, e202116965.

[41] Fenger, R.; Fertitta, E.; Kirmse, H.; Thünemann, A. F.; Rademann, K. Size dependent catalysis with CTAB-stabilized gold nanoparticles. *Phys. Chem. Chem. Phys.* **2012**, *14*, 9343–9349.

[42] Liang, M.; Su, R. X.; Huang, R. L.; Qi, W.; Yu, Y. J.; Wang, L. B.; He, Z. M. Facile *in situ* synthesis of silver nanoparticles on procyanidin-grafted eggshell membrane and their catalytic properties. *ACS Appl. Mater. Interfaces* **2014**, *6*, 4638–4649.